

FREQUENCY-DEPENDENT NATURE OF P_n IN WESTERN CHINA

Robert L. Nowack¹, Wang-Ping Chen², and Tai-Lin Tseng²

Purdue University¹ and University of Illinois²

Sponsored by the Air Force Research Laboratory

Award No. FA8718-08-C-0025

Proposal No. BAA08-42

ABSTRACT

We are investigating P_n propagation in Western China based on regional events recorded by the Hi-CLIMB (An Integrated Study of the Himalayan-Tibetan Continental Lithosphere during Mountain Building) array in the region. Seismic attributes, including arrival times, Hilbert envelope amplitudes and instantaneous and spectral frequencies, are being used to investigate how the crustal and upper mantle velocity and attenuation structure affects the propagation of P_n arrivals in Tibet. We have constructed more than 30 high-quality regional seismic profiles, and of these, 14 events have been selected with excellent crustal and P_n arrivals for further analysis. Regional travel-times recorded by the Hi-CLIMB array are used to constrain the larger scale velocity structure in the region, with four events near the array used to constrain the crustal structure. We are also independently constraining the variation of upper mantle velocity and depth of the Moho by modeling SV -coupled shear waves at teleseismic distances. The amplitude of the $SsPmP$ phase is particularly sensitive to upper mantle velocities when it is near critical. The initial modeling of the $SsPmP$ phase indicates that the Moho beneath southern Lhasa is over 75 km deep with P_n velocities greater than 8 km/s. In contrast, the data sampling the Qiangtang terrane north of the Bangong-Nujiang suture shows thinner crust with P_n velocities less than 8 km/s. This is generally consistent with the results from the P_n travel-times for regional events recorded on the Hi-CLIMB array. Nonetheless, there is additional variability of the regional travel-time data, suggesting further 3D complexities. Seismic amplitude and frequency attributes are being extracted from the crustal and P_n wave-trains, and these data are being compared with numerical and analytical results for models with upper mantle velocity gradients, which can strongly affect P_n amplitudes and frequencies. The numerical modeling is performed using approximate ray and beam methods and the more complete spectral element method (SEM). The results from the SEM method are in good agreement with analytical and reflectivity results for different models with upper mantle velocity gradients. Using the SEM method, we are testing the effects of random crustal and Moho depth heterogeneities to see how this variability impacts the range of P_n attributes observed. Ultimately the approach we are following is a mostly data-driven analysis of P_n seismic attributes in order to investigate the trade-offs of large scale lithospheric structure, small scale heterogeneities and attenuation in Tibet.

OBJECTIVES

We are analyzing the propagation of regional Pn waves recorded by Hi-CLIMB in Tibet. Considering the station-spacing (3 to 8 km) and large aperture (800 km) of the Hi-CLIMB seismic experiment, our objective is to use these densely recorded data to construct a self-consistent model of Pn propagation over a large region in western China. In turn, a better understanding of the effects of propagation from analysis of the data will improve frequency dependent attenuation models of regional Pn phases, leading to a clearer separation of elastic and anelastic effects in a laterally varying crust and upper mantle, eventually eliminating the assumption of a simplified, frequency-independent geometric spreading component.

To account for the intricate nature of Pn propagation, we are applying fast ray and beam methods (Nowack and Stacy, 2002), as well as SEM (Komatitsch and Vilotte, 1998; Komatitsch et al., 2005). In contrast, alternatives such as the reflectivity method, are restricted to 1D media. SEM can be applied in 2D or 3D and implemented in parallel using MPI on large cluster computing. Ray and beam methods are faster and can provide asymptotic results appropriate when a large number of forward calculations are required, such as in large-scale inversions. However, for small-scale scattering, complete numerical methods, such as SEM, may be more appropriate. As a practical measure, essential features of Pn waveforms are being distilled into seismic attributes including arrival times, envelopes of wave amplitudes, and pulse frequencies for modeling and inversion.

RESEARCH ACCOMPLISHED

We have constructed more than 30 high-quality seismic profiles recorded on the Tibet Hi-CLIMB array and from these 14, have been selected for further analysis. Similarities in the seismic profiles for events in clusters are outstanding. About two thirds of the larger earthquakes have fault plane solutions available in the global Harvard Centroid Moment Tensor (CMT) catalog (Dziewonski et al., 1981) and the report by Baur (2007). For those without fault plane solutions, we have identified the ones that can potentially be resolved using regional waveforms recorded by Hi-CLIMB stations for their appropriate azimuthal coverage, or by using teleseismic waveforms (Figure 1). The analysis of moment tensor inversion is in progress. The fault plane solutions that cannot be obtained through this method may be roughly estimated based on geologic structures or historic solutions.

As a complimentary approach to the analysis of regional seismograms, we are independently constraining the variation of upper mantle velocity and the depth of Moho by modeling shear waveforms at teleseismic distances shorter than 50 degrees. In essence, the amplitude of the SV -coupled P phase $SsPmp$ is very sensitive to the upper mantle velocities when the rays hit the Moho near the critical angle. Our results indicate that the significant decrease in amplitude of $SsPmp$ near northern Hi-CLIMB stations can be explained by slow velocity anomalies in the uppermost mantle beneath northern central Tibet.

Regional events recorded by the Tibet Hi-CLIMB array with locations approximately in-line with the array have been chosen for initial analysis. However, other events in specific terranes have also been selected for later processing. Four of the in-line events have epicenters less than 200 km from the Hi-CLIMB array; these events were relocated with data from the Hi-CLIMB array using the earthquake location program HYPOINVERSE-2000 (Klein, 2002). The locations of selected in-line events are shown in Figure 2, using the EHB (Engdahl et al., 1998) or the Preliminary Determination of Epicenters (PDE) catalogs for all events except for the four nearby events (L2a, L2d, L3a and L3b), which were relocated using Hi-CLIMB data. These relocations improved the fit to the travel-times, but moved the epicenters by less than 5 km. For more distant events in Tibet, a focal depth normalization procedure was used since events on Tibetan plateau are dominantly less than 15 km in focal depth (e.g., Molnar and Chen, 1983; Chen and Molnar, 1983; Langin et al., 2003).

The observed arrival times for the four nearby events were then used to refine the crustal velocity model beneath the array with the 3D ray tracing code CRT (ver. 6.0) using the approach described by Cerveny et al. (1988). The calculated travel-times were compared with the observed arrival times in order to iteratively refine the crustal velocity model. The initial velocity model was based on seismic refraction analysis of controlled shots for the INDEPTH III experiment by Meissner et al. (2004). It was found that the relocated nearby events combined with the refined crustal velocity model provide a reasonable fit to the observed crustal travel-times. An example of the observed and calculated travel-times for nearby event L3a is shown in Figure 3.

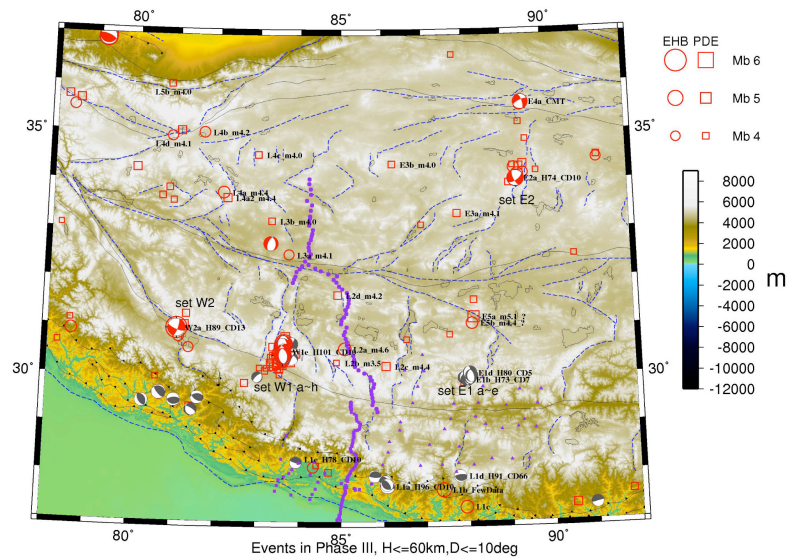


Figure 1. Map of the Hi-CLIMB array with selected labeled events for which seismic profiles have been constructed. The red focal mechanisms were obtained from the global CMT catalog and the gray ones from Baur (2007).

In order to model the *Pn* phase arrival times, work is currently being performed to pick the *Pn* branches and refine the Moho depths. An example of the ray tracing for the *Pn* diving ray for the southern event L1a is shown in Figure 4. For events such as L1a, located along the Himalayan front, the *Pn* arrival times are complicated. There exist rapid variations of Moho depth with a shallowing of the Moho along the Himalayan front and south to the Indian shield. The Lhasa terrane in the central Tibetan plateau has a much greater Moho depth, and north of the Bangong-Nuijiang suture in the Qiangtang terrane of Tibet, the Moho moderately shallows. After modeling all the *Pn* arrival times, the other seismic attributes will be modeled, including seismic amplitudes and pulse frequencies

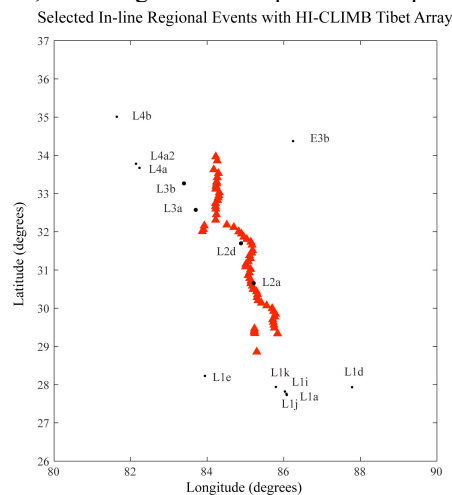


Figure 2. Selected regional events approximately in-line with the Hi-CLIMB Tibet seismic array.

For examples of shot profiles with longer *Pn* branches, we have modeled the travel-times for event L1e to the south and event E3b to the north of the Hi-CLIMB array. The left plot of Figure 5 shows the travel-times for event

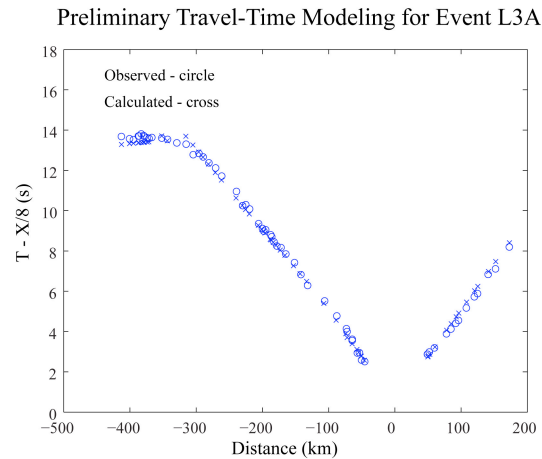


Figure 3. Initial travel-time modeling of Event L3a to constrain crustal structure beneath the Hi-CLIMB array in Tibet.

L1e, where the circles are the observed times and the crosses are calculated times using the 3D ray tracer CRT for the preliminary model shown in the right plot. Similar to the modeling of travel-times for the nearby events to the array, the crustal phases for distances <260 km for event L1e are relatively slow down to the Moho. The modeling of the Pn branch shows a deepening of the Moho from the Himalayan front down to 75 km for the Lhasa terrane in central Tibet with Pn speeds between 8.2 and 8.3 km/s. Then, to the north of the Bangong-Nujiang suture (BNS) in the Qiantang terrane, the Moho shallows by about 10 km to 63–65 km with slower Pn speeds of about 7.8 km/s. In the left plot of Figure 5, the Pn branch is first, resulting from the deepening Moho, and then becomes earlier resulting from the thinning of the crust to the north. The upper mantle gradient inferred from the modeling is about 0.003 to 0.004 km/s per km consistent with the work of Philips et al. (2007) for the region.

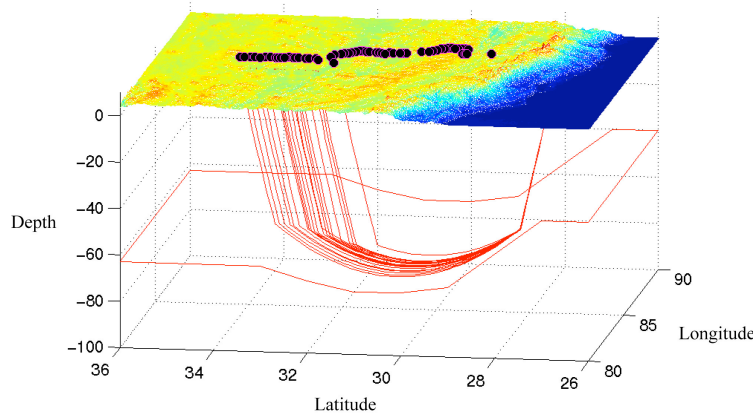


Figure 4. An example of 3D ray tracing of the diving Pn phase for event L1a using a Tibet model with a highly variable Moho topography

The second event-gather to be modeled is from Event E3b located to the north of the Hi-CLIMB array (shown in Figure 2). The travel-times are shown in the left plot of Figure 6 where the circles are the observed times and the crosses are the calculated times using the 3D ray tracer CRT and the preliminary model is shown in the right plot. Again the crust is relatively slow down to the Moho with no indication of a higher velocity lower crust. The Pn branch then arrives initially early, indicating the shallower Moho to the north and then is delayed, resulting from the deeper Moho in the Lhasa terrane in central Tibet. However, to match the complete travel-time curve, a slower Pn speed is required to the north with the Pn speed increasing to the south as the Moho deepens. The modeling of this event located north of the array is consistent with the modeling of event L1e to the south of the array. For the

modeling of both event-gathers, upper mantle gradients of between 0.003 and 0.004 km/s per km are consistent with the data and similar to the results found by Philips et al. (2007) for the region.

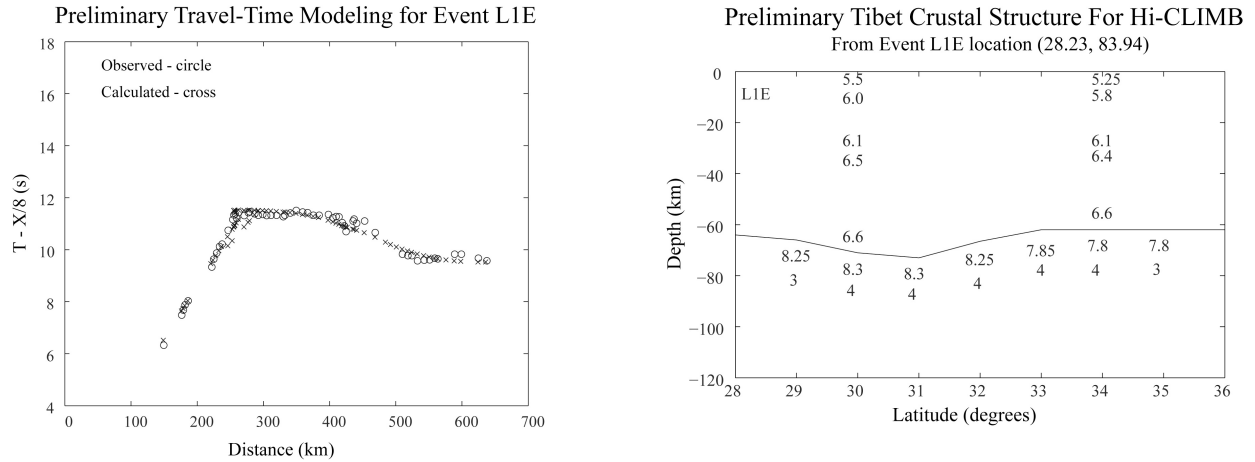


Figure 5. Initial travel-time modeling of Event L1e to constrain upper mantle structure near the Hi-CLIMB array in Tibet. The left plot shows the observed (circles) and calculated (crosses) travel-times. The right figure shows the initial crustal and upper mantle model in the vicinity of the Hi-CLIMB array from travel-time modeling for event L1e. Velocities are shown in km/s and single digits show upper mantle velocity gradients in units of 0.001 (km/s per km).

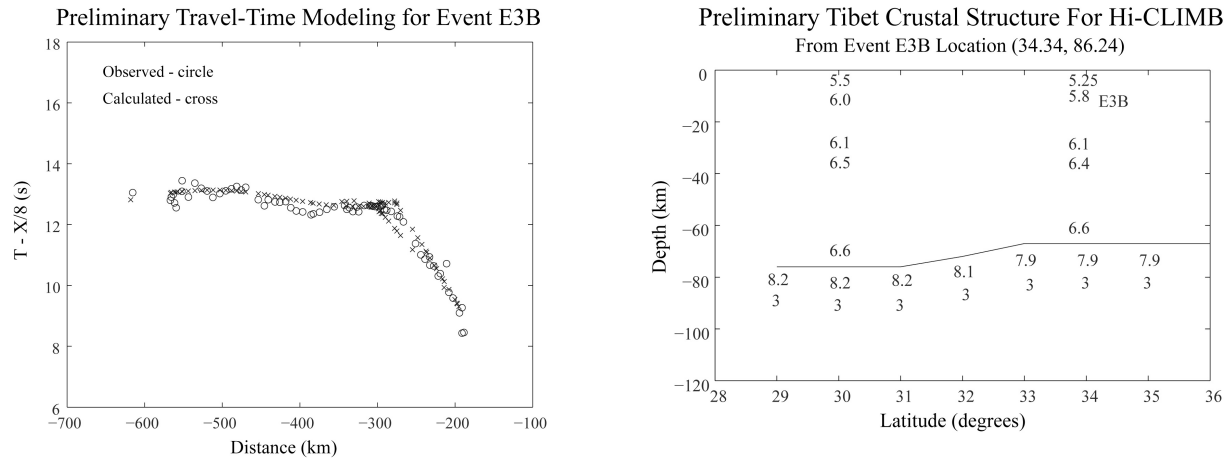


Figure 6. Initial travel-time modeling of Event E3b to constrain upper mantle structure near the Hi-CLIMB array in Tibet. The left plot shows the observed (circles) and calculated (crosses) travel-times. The right figure shows the initial crustal and upper mantle model in the vicinity of the Hi-CLIMB array from travel-time modeling for event L1e. Velocities are shown in km/s and single digits show upper mantle velocity gradients in units of .001 (km/s per km).

As a preliminary example of seismic amplitudes, Figure 7 shows the Hilbert envelope amplitudes for Event L1e. The dots in the figure are envelope amplitudes obtained from a two second window after the arrival times. The lines are curves proportional to $1/R$ and $1/(R^2)$ set to be equal at 200 km. Between distances of about 260–340 km, the P_n amplitudes are lower and then increase to between 340 to 425 km. After 425 km and north of the BNS in the Qiantang terrane, the P_n amplitudes decrease relative to the two decay curves. Since the Moho decreases in depth by about 10 km across the BNS, the amplitudes for event L1e suggest that large scale structural features are influencing the amplitude attributes. Nonetheless, the Moho structure beneath the Himalayas and Tibet is complicated and more analysis is needed to interpret the observed seismic attributes on the different seismic profiles. We are still analyzing

the results for pulse frequency attributes, as well as the decay of amplitudes with distance. However, we are applying a data driven approach to interpret the trade-offs between structural effects of the medium as opposed to other attenuation effects, and not driven by an assumed model for the analysis of the observed seismic attributes. In any case, large-scale structural features need to be taken into account for the modeling of seismic attributes, such as amplitudes and pulse frequencies, in addition to the modeling of scattering from small scale features and intrinsic attenuation.

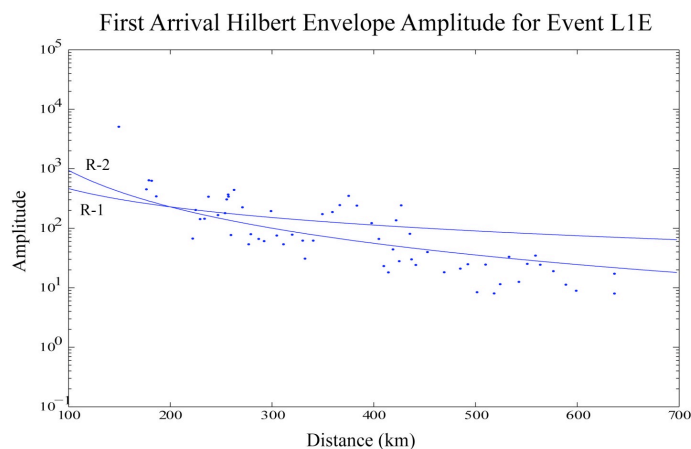


Figure 7. Hilbert envelope amplitudes of first arrivals for Event L1E. The two lines illustrate R-1 and R-2 decay curves shown to coincide with the data at 200 km. Note that after 250 km the amplitudes first decay and then get larger from 350 to 430 km. For distances greater than 450 km, the amplitudes are lower again, possibly correlated with the Bangong-Nujiang Suture in Tibet.

We are currently performing numerical simulations of elastic wave solutions for later comparison with the observed data. We have implemented SEM using the parallel code Specfem2d for the simulation of 2D viscoelastic and anisotropic media (Komatitsch and Vilotte, 1998; Komatitsch et al., 2005). This code allows us to use the cluster computing facilities available at Purdue University and the University of Illinois. These SEM calculations let us compare with asymptotic ray and beam calculations and gain insight into the parameters that affect the P_n arrivals, including crustal and upper mantle velocities and gradients, lateral variability in the Moho depth, and small scale scattering and intrinsic attenuation in the crust and upper mantle.

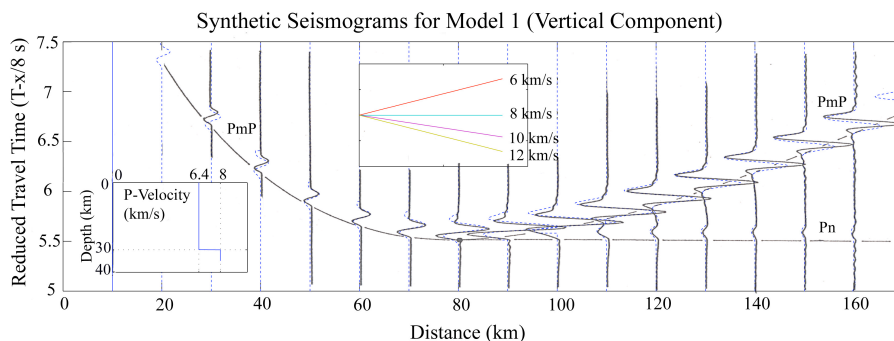


Figure 8a. Comparison between the results from SEM (dotted) and the reflectivity results (solid) of Braile and Smith (1975) for a constant velocity 30 km crust over a constant velocity mantle. The amplitudes of the reflectivity results are multiplied by distance and the SEM results are multiplied by the square-root of distance.

Figure 8a shows an example synthetic record section for a model with a 6.4 km/s crust, a sharp discontinuity at the Moho and a constant 8.0 km/s mantle. The times are reduced by 8.0 km/s. The P_mP reflected waves and P_n head waves are designated on the record section. The solid lines are the seismograms computed using the reflectivity method by Braile and Smith (1975) and the dotted lines are our calculations using SEM modeling, where the

amplitudes are scaled by distance for the reflectivity calculation and by the square root of the distance for the 2D SEM synthetics. The comparison between them is very good, and suggests that we are implementing the SEM code correctly. Note the small amplitude of the pure head wave phase on the synthetics in this ideal case.

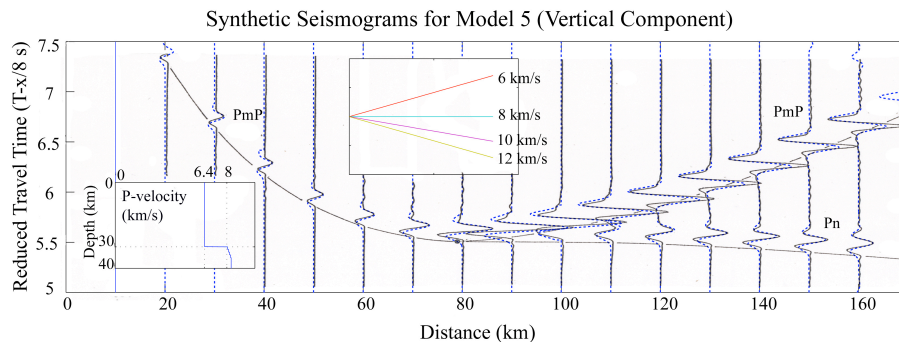


Figure 8b. This shows a comparison between the results from our spectral element calculation (dotted) and the reflectivity results (solid) of Braile and Smith (1975) for a constant velocity 30 km crust over a mantle with a velocity gradient in the top 5 km. The amplitudes of the reflectivity results are multiplied by distance and the SEM results are multiplied by the square-root of distance.

Figure 8b shows an example of synthetic seismograms for a velocity model with an upper mantle gradient in the first 5 km below the Moho. This model is referred to as Moho-5 in Braile and Smith (1975). The solid seismograms are from the reflectivity calculations of Braile and Smith (1975) and the dotted seismograms are from our calculations using the SEM modeling. The reflectivity amplitudes are multiplied by distance and the SEM results are multiplied by the square root of distance. Again, the comparison between the two results is very good, suggesting that we are implementing the SEM modeling correctly. Note the large *Pn* amplitudes resulting from the upper mantle gradient in contrast to the ideal head wave case in Figure 8a. Even in the 1970s, it was recognized that there was a trade-off between large-scale structural features, such as upper mantle velocity gradients and other forms of seismic attenuation.

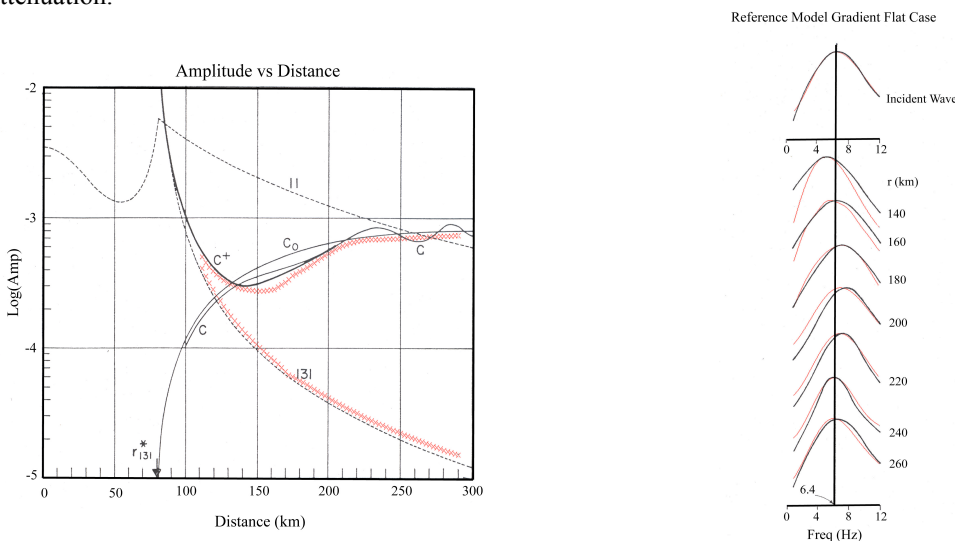


Figure 9. The left plot shows a comparison of the spectral element results (red crosses) with the asymptotic results of Cerveny and Ravindra (1971) for a layer over a halfspace (131 curve) and for a C+ interference head wave for a layer over a velocity gradient. The background curves are from Cerveny and Ravindra (1971). The right plot shows the amplitude spectra, where the black curves are from Cerveny and Ravindra (1971) and the red curves are from the SEM results. Pulse distances for the spectra are shown to the right.

The left plot of Figure 9 shows a comparison between the log-amplitudes from the SEM calculations and the asymptotic results are from Cerveny and Ravindra (1971) for a layer over a half space and a layer over a velocity gradient. The Moho is at a depth of 30 km with a contrast of 6.4 km/s over 8 km/s. For the velocity gradient case, the gradient is 0.02264 km/s per km. This is larger than typically observed mantle gradient values (0.001 and .005 km/s per km) but decreases the distance range for different frequency and amplitude effects to occur, making it more efficient for numerical calculations. Note that the flattening of a spherical earth will result in an effective velocity gradient of about 0.001 km/s per km in the flattened Earth (Yang et al., 2007). The background figure is from Cerveny and Ravindra (1971) where the C+ wave is the interference head wave, the Co wave is the pure diving wave and the 131 wave is the pure head wave case. The red crosses are from the SEM calculations for the interference and pure head wave cases. For the asymptotic results of Cerveny and Ravindra (1971), the amplitude blows up at the critical distance near 80 km and the comparisons are shown only for distances greater than 110 km. For the C+ interference head wave, the amplitude initially decreases after the critical distance and then recovers as the diving wave becomes the dominant wide-angle wave. There are some undulations in the asymptotic results of Cerveny and Ravindra (1971) for distances greater than 220 km for the C+ wave that are not seen in the SEM calculations, but otherwise the results of the SEM calculations are reasonably consistent.

The right plot of Figure 9 shows the amplitude spectra as a function of distance for the interference head wave. The black curves are from Cerveny and Ravindra (1971), and the red curves are from the SEM calculations for the same layer over a velocity gradient model. Both results show that the dominant frequency initially decreases at 140 km with the maximum of the amplitude spectrum less than that of the incident wave because of the frequency decrease of the pure head wave. As the diving wave begins to emerge, the dominant frequency increases. However, because of tuning effects between the different interference waves, the dominant frequency overshoots that of the incident wave to higher frequencies. This was also found by Nowack and Stacy (2002) using both Gaussian beams and reflectivity calculations.

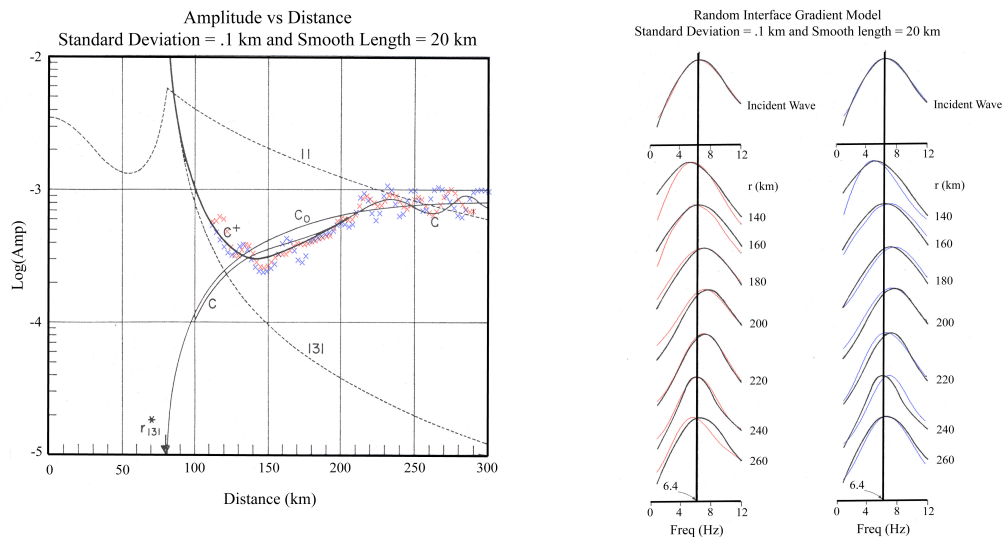


Figure 10. The left figure shows a comparison of the SEM results (red crosses) with the asymptotic results of Cerveny and Ravindra (1971) for a layer over a velocity gradient. The red and the blue crosses are for the random perturbations on the Moho shown in Fig. 11. The background curves are from Cerveny and Ravindra (1971). The right figure shows the amplitude spectra for the two perturbed Moho interfaces for a layer over a velocity gradient. The black curves are from Cerveny and Ravindra (1971) and the red and blue curves are from the SEM results. Pulse distances for the spectra are shown to the right.

The left plot of Figure 10 shows the amplitude comparison between SEM calculations for two random Moho interfaces with a standard deviation of 0.1 km and a smoothing length of 20 km with the unperturbed, asymptotic

results of Cerveny and Ravindra (1971) for a layer over a velocity gradient. Normal random numbers are first generated in Matlab and then are smoothed using three passes of a boxcar smoothing of length 6.5, 6.5 and 7 km in order to smooth out the higher wavenumbers. The right plot of Figure 10 shows the effect of two random perturbations of the Moho depth on the pulse spectra at different distances. The results show that the main features of the C+ interference wave are preserved for small perturbations of the Moho depth. Numerical results for longer smoothing lengths for the perturbation, but the same average vertical deviation, show similar results but with longer average wavenumbers for the amplitude perturbation. Numerical examples with a standard deviation of 0.25 km in vertical depth perturbation of the Moho shows larger perturbations of the interference head wave amplitude but still vary about the main feature trend of the reference case. Nonetheless, preliminary calculations with larger scale structure features have more significant effects on the amplitude and frequency characteristics of the P_n wave and will be investigated in the future.

CONCLUSIONS AND RECOMMENDATIONS

We have assembled a number of record sections from regional events recorded by the Hi-CLIMB array. For several events nearby the Hi-CLIMB array, we have relocated the events using Hi-CLIMB data. For more distant events in Tibet, a focal depth normalization procedure has been used since events on the Tibetan plateau are dominantly less than 15 km in focal depth (e.g., Molnar and Chen, 1983). From these record sections, seismic attributes of the P_n phase are being extracted from the data, including arrival times, envelope amplitudes and instantaneous and spectral pulse frequencies. Several nearby events to the Hi-CLIMB array have been used to constrain crustal velocities from crustal branches. For the P_n phase, the travel-times are being modeled using 3D ray tracing in order to constrain large scale structural features including Moho depths, upper mantle velocities and velocity gradients. The modeling of travel-times for all the selected event gathers will result in an integrated 3D model for the region. Also, teleseismic analysis of the $SsPmp$ phase is being performed to further constrain the crustal and upper mantle structure.

Numerical modeling is performed using the spectral element method (SEM) in order to compare the effects of large-scale crustal structure on seismic attributes. For the layer over a velocity gradient case, the SEM results compare favorably with the asymptotic results of Cerveny and Ravindra (1971) and the reflectivity calculations of Braile and Smith (1975). Seismic amplitude and pulse frequency results using SEM are stable for small interface perturbations. Lay et al. (2008) reported more drastic variations obtained from finite difference modeling for upper mantle velocity perturbations. Presumably these results occur since the mantle velocity perturbations change the upper mantle gradients, which control the primary properties of the interference head wave. Nonetheless, larger variations of Moho depth have more pronounced focusing and defocusing effects on P_n amplitudes than shown here. We are starting to perform SEM tests for large scale structural models that occur in Tibet and these are anticipated to have strong effects on the properties of the P_n wave.

REFERENCES

- Baur, J. R. (2007). Seismotectonics of the Himalayas and the Tibetan Plateau: moment tensor analysis of regional seismograms, M.S. thesis, Oregon State University.
- Braile, L. W. and R. B. Smith (1975). Guide to the interpretation of crustal refraction profiles, *Geophys. J.R. Astr. Soc.* 40: 145–176.
- Cerveny, V., L. Klimes, and I. Psencik (1988). Complete Seismic-Ray Tracing in Three-Dimensional Structures. In *Seismological Algorithms*, London: Academic Press: 89–168
- Cerveny, V. and R. Ravindra (1971). *Theory of Seismic Head Waves*, Univ. of Toronto Press.
- Chen, W.-P., and P. Molnar (1983). Focal depths of intracontinental and intraplate earthquakes and their implications for the thermal and mechanical properties of the lithosphere, *J. Geophys. Res.* 88: 4183–4214.
- Dziewonski, A. M., T.-A. Chou and J. H. Woodhouse (1981). Determination of earthquake source parameters from waveform data for studies of global and regional seismicity, *J. Geophys. Res.* 86: 2825–2852.
- Engdahl, E. R., R. D. van der Hilst, and R.P. Buland (1998). Global teleseismic earthquake relocation with improved travel times and procedures for depth determination, *Bull. Seism. Soc. Am.* 88: 722–743.

2009 Monitoring Research Review: Ground-Based Nuclear Explosion Monitoring Technologies

- Klein, F. (2002). HYPOINVERSE-2000 (4/2002 vers.) [Computer Software]. Menlo Park, CA: U.S. Geological Survey.
- Komatitsch, D. and J. P. Vilotte (1998). The spectral element method: an efficient tool to simulate the seismic response of 2D and 3D geological structures, *Bull. Seismol. Soc. Am.* 88: 368–392.
- Komatitsch, D., S. Tsuboi and J. Tromp (2005). The spectral-element method in seismology, in *Seismic Earth: Array Analysis of Broadband Seismograms*, (Eds. A. Levander and G. Nolet), Geophysical Monograph Series, Vol. 157, American Geophysical Union, Washington D.C.: 205–227.
- Langin, W. R., L. D. Brown, and E. A. Sandvol (2003). Seismicity of central Tibet from Project INDEPTH III seismic recordings, *Bull. Seism. Soc. Am.* 93: 2146–2159.
- Lay, T., X. B. Xie and X. Yang (2008). Development of regional phase tomographic attenuation models for Eurasia, in *Proceedings of the 30th Monitoring Research Review: Ground-Based Nuclear Explosion Monitoring Technologies*, LA-UR-08-05261, Vol. 1, pp. 98–107.
- Meissner, R., F. Tilmann, and S. Haines (2004). About the lithospheric structure of central Tibet, based on seismic data from the INDEPTH III profile, *Tectonophysics* 380: 1–25.
- Molnar, P. and W.-P. Chen (1983). Depths and fault plane solutions of earthquakes under the Tibetan plateau, *J. Geophys. Res.* 88: 1180–1196.
- Nowack, R. L. and S. M. Stacy (2002). Synthetic seismograms and wide-angle seismic attributes from the Gaussian beam and reflectivity methods for models with interfaces and velocity gradients, *Pure Appl. Geophys.* 159: 1447–1464.
- Phillips, W. S., M. L. Begnaud, C. A. Rowe, L. K. Steck, S. C. Myers, M. E. Pasyanos, and S. Ballard (2007). Accounting for lateral variations of the upper mantle gradient in Pn tomography studies, *Geophys. Res. Lett.* 34: doi:10.1029/2007GL029338.
- Yang, X., T. Lay, X. B. Xie, and M. S. Thorne (2007). Geometric spreading of Pn and Sn in a spherical earth model, *Bull. Seism. Soc. Am.* 97: 2053–2065.